Copyright WILEY-VCH Verlag GmbH & Co. KGaA, 69469 Weinheim, Germany, 2020.

ADVANCED OPTICAL MATERIALS

Supporting Information

for *Adv. Optical Mater.*, DOI: 10.1002/adom.202000337

High-Responsivity Mid-Infrared Black Phosphorus Slow Light Waveguide Photodetector

*Yiming Ma, Bowei Dong, Jingxuan Wei, Yuhua Chang, Li Huang, Kah-Wee Ang, and Chengkuo Lee**

Copyright WILEY-VCH Verlag GmbH & Co. KGaA, 69469 Weinheim, Germany, 2020.

Supporting Information

High-Responsivity Mid-Infrared Black Phosphorus Slow Light Waveguide Photodetector

*Yiming Ma, Bowei Dong, Jingxuan Wei, Yuhua Chang, Li Huang, Kah-Wee Ang, and Chengkuo Lee**

Contents

Note S1: Angular-resolved polarized raman spectroscopy

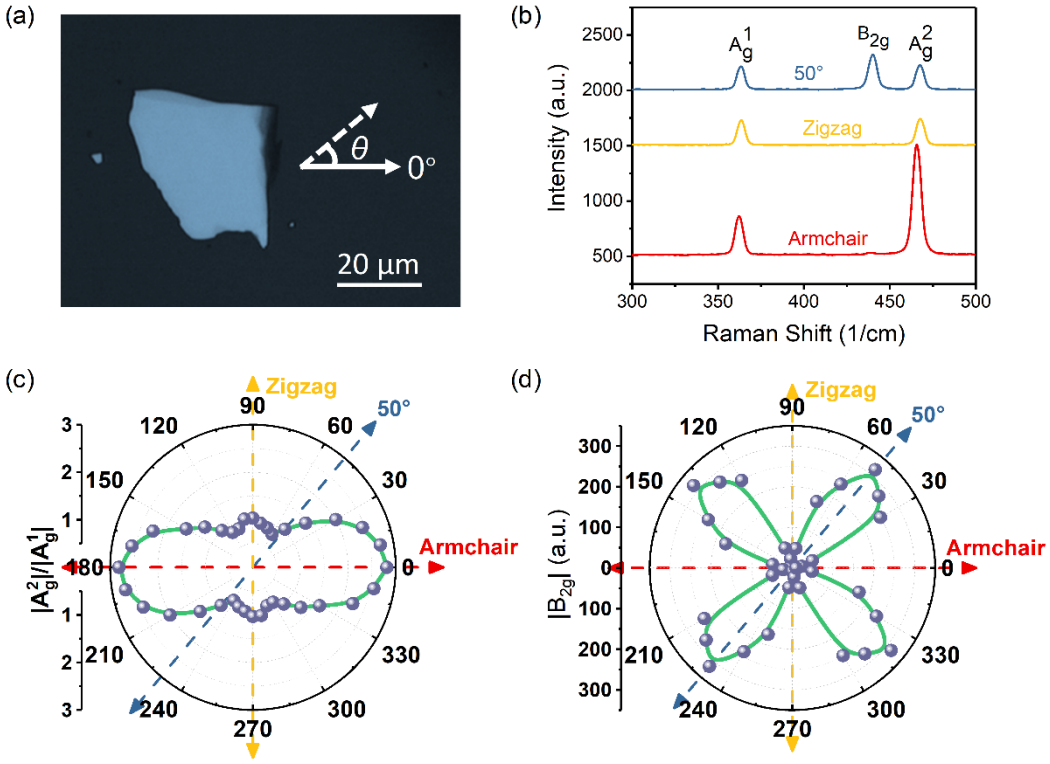

Figure S1. Angle-resolved polarized Raman spectroscopy in parallel configuration on a 27 nm BP flake exfoliated on a silicon substrate. (a) Microscopic image of the BP flake. (b) Polarized Raman spectra at different polarization angles. (c) Polar plot of A_g^2/A_g^1 Raman intensity ratio as a function of polarization angle. (d) Polar plot of B_{2g} Raman intensity as a function of polarization angle.

Figure S1 shows the angle-resolved polarized Raman spectroscopy in parallel configuration (the incident laser polarization parallel with the detection polarization) on a 27 nm BP flake exfoliated on a heavily doped silicon substrate covered with 90 nm SiO_2. As illustrated in Figure S1c, the A_g^2/A_g^1 Raman intensity ratio shows a variation period of 180°, with a maximum along the armchair direction and a second maximum along the zigzag direction. Meanwhile as shown in Figure S1d, the B_{2g} Raman intensity has a variation period of 90° and is completely forbidden along the armchair and zigzag directions. These results are consistent with those reported in previous works,[1–3] and prove that it is a simple yet effective

and accurate method to determine the BP crystal orientations by firstly finding out the polarization angle in parallel configuration where the B_{2g} peak vanishes then distinguishing the armchair and zigzag orientations according to the A_g^2/A_g^1 intensity ratio, as shown in Figure S1b. In the parallel configuration, the B_{2g} mode can be filtered out when either the armchair or zigzag axis of BP is aligned with the laser polarization. To further distinguish these two axes, we looked into the A_g^2/A_g^1 Raman intensity ratio in the parallel configuration. The armchair-oriented atomic vibrations of A_g^2 phonons lead to maximized A_g^2 Raman intensity when the laser polarization is along the armchair direction, while the A_g^1 Raman intensity remains unchanged as the A_g^1 phonon vibrate out-of-plane. Therefore, the A_g^2/A_g^1 Raman intensity ratio is larger with armchair-polarized laser excitation and smaller with zigzag-polarized laser excitation, which serves as Raman signatures of armchair and zigzag lattice axes.

Note S2: Transmission spectra of waveguide systems

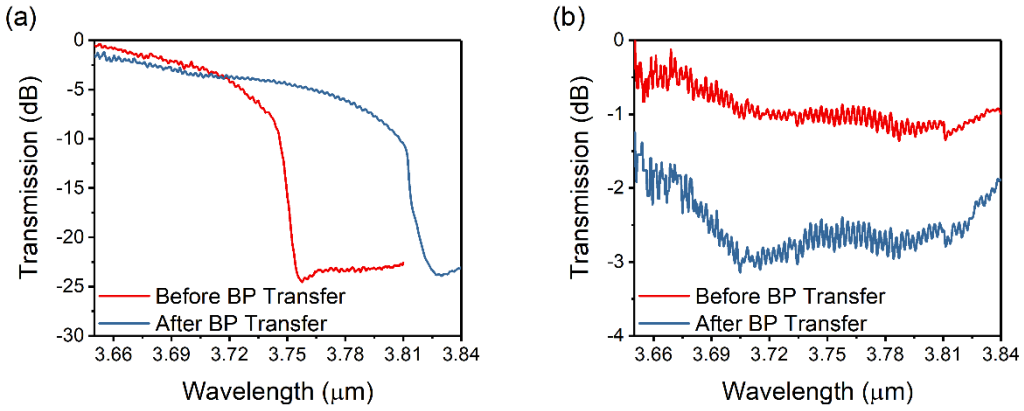

Figure S2. Transmission spectra of (a) the PhCWG system; (b) the SWGWG system, before and after the BP transfer process.

Note S3: BP polarization-resolved extinction spectra and absorption coefficient

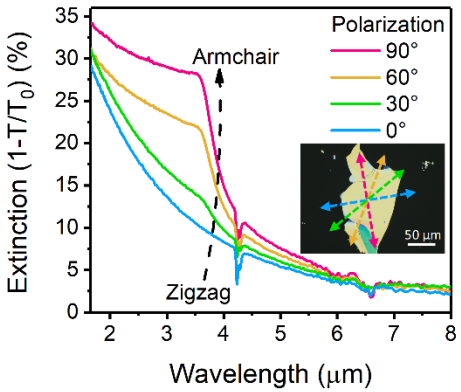

Figure S3. Polarization-resolved extinction spectra of a 40 nm BP flake on a CaF_2 substrate with light polarized along the four directions as shown in the inset. Inset: microscopic image of the BP flake.

Figure S3 shows the polarization-resolved extinction spectra of a 40 nm BP flake on a CaF_2 substrate measured by Fourier transform infrared spectroscopy (FTIR). CaF_2 is transparent up to 8 μm. It is seen that the BP absorption decreases with the increasing wavelength and drops dramatically beyond the roll-off wavelength of ~3.6 μm along the armchair direction. These trends agree well with the BP extinction spectra reported in previous works.[4,5]

Table S1. Comparison of BP absorption coefficients on waveguides

Wavelength (μm)	**BP Flake Thickness (nm)**	**BP Absorption Coefficient (dB/μm)**	**BP Absorption Percentage (%)**	**Ref.**
1.55	11.5	0.182	-	[6]
2	36.8	0.105	23.96	[7]
3.825	40	0.041	8.99	This work

Table S1 compares the BP absorption coefficient in this work and those in two previous works, where the zigzag orientation of BP is also aligned with the waveguide propagation

direction. The BP absorption percentages are extracted from Figure S3. The BP absorption coefficient in this work is among the lowest because of the longest wavelength. If we calculate the BP absorption coefficient at 3.825 μm according to the reported value at 2 μm and the ratio of the BP absorption percentages at these two wavelengths, a value of 0.039 dB/μm is derived, which is slightly lower than our measured value as our BP flake is a bit thicker. Therefore, our measured BP absorption coefficient is in good agreement with the reported values, indicating that the interaction between the BP flake and the light propagating in the waveguides is efficient in our devices.

Note S4: Group indices of ridge waveguide and SWGWG

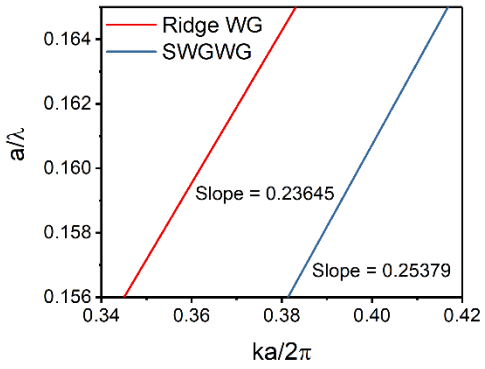

Figure S4. Dispersion curves of the ridge waveguide in the reference arm of the MZI, and the SWGWG after the BP transfer process.

The dispersion curves were calculated by the plane wave expansion method using the MIT photonic bands (MPB) software. The slope of the dispersion curve represents the group velocity, which is nearly constant over the studied wavelength range of 3.65-3.84 μm in both waveguides. Thus, the group index is the reciprocal of the slope and is 4.23 and 3.94 for the ridge waveguide in the MZI reference arm and the SWGWG after the BP transfer process, respectively.

Note S5: Calibration of power on BP photodetectors

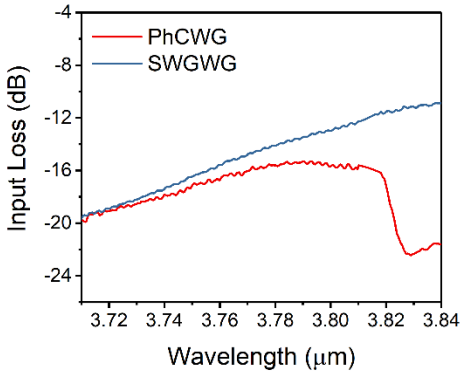

Figure S5. Loss from the input fiber to the input port of the BP PhCWG/SWGWG photodetector.

The incident power to the BP waveguide photodetector was calibrated from the total loss from the input fiber to the input port of the photodetector, which consists of the losses of the input fiber, the input grating coupler, and the input ridge waveguide, and the reflection loss at the input port of the PhCWG or the SWGWG. The fiber loss was obtained by measuring the power at the input and output of the fiber using a power meter. The on-chip losses were characterized before the BP transfer process by normalizing the transmission spectrum of the on-chip system to that of an off-chip light path. The losses of the input side and the output side of the system are equal due to its symmetry. The propagation losses of the PhCWG and the SWGWG are negligible because of their short length of only 10 μm. The reflection loss at the input port is caused by the mode mismatch between the ridge waveguide and the PhCWG/SWGWG, which origins primarily from the structural dispersion rather than the material dispersion. As a result, the effect of the thin BP flake to the reflection loss at the input port of the PhCWG/SWGWG is negligible. Consequently, the loss from the input fiber to the input port of BP PhCWG/SWGWG photodetector can be extracted, as shown in Figure

S5. Based on these loss values, the incident power to the BP photodetector can be fixed by adjusting the incident power to the input fiber accordingly.

Note S6: Relationship between photocurrent and bias

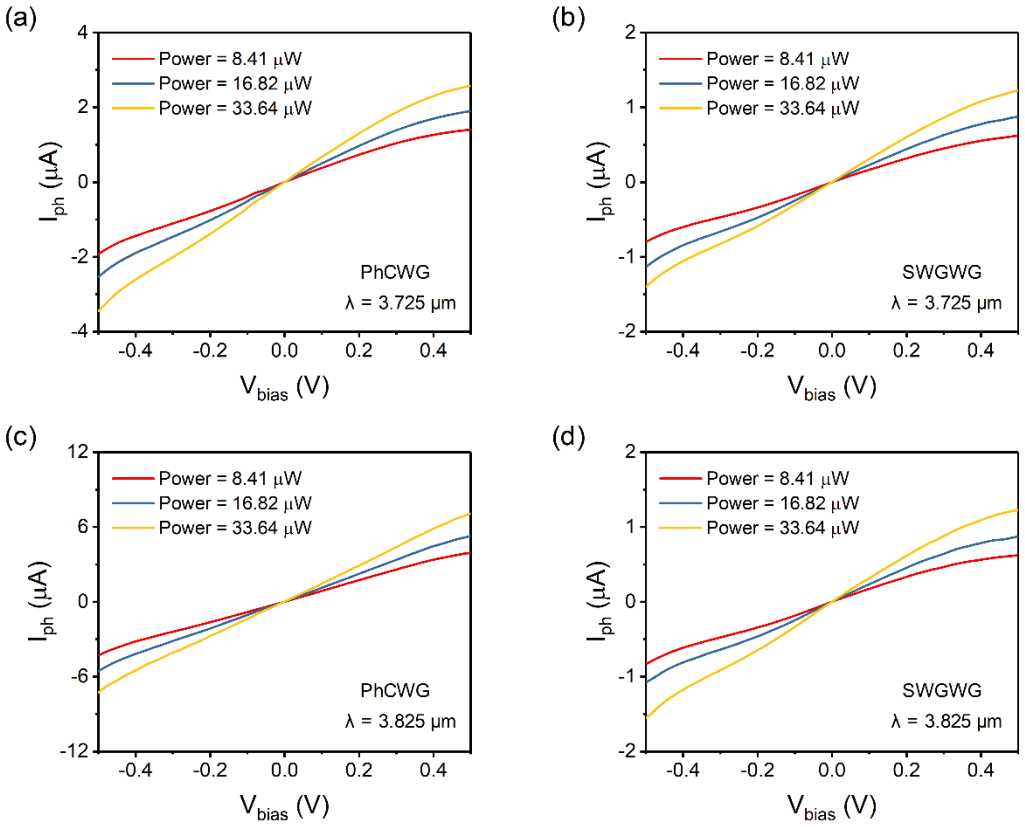

Figure S6. Relationship between photocurrent and voltage bias under varying incident power in (a) BP PhCWG photodetector at 3.725 μm; (b) BP SWGWG photodetector at 3.725 μm; (c) BP PhCWG photodetector at 3.825 μm; (d) BP SWGWG photodetector at 3.825 μm.

Note S7: Dark current, shot noise and Johnson noise

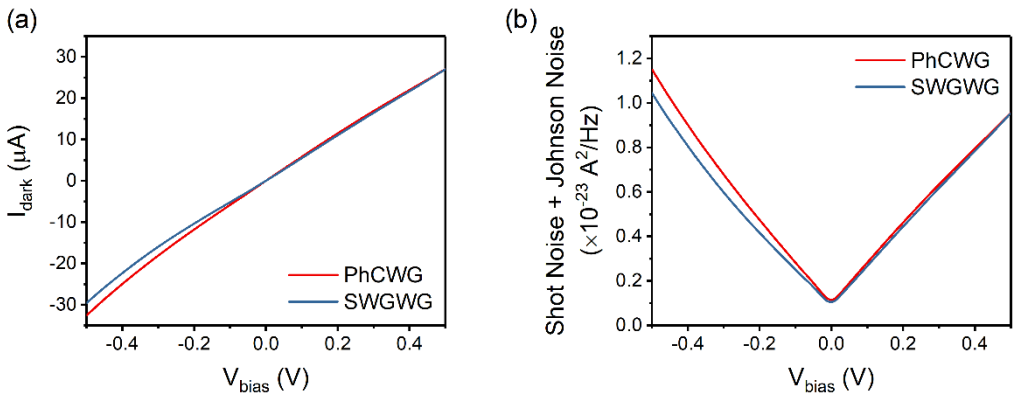

Figure S7. (a) Dark current and (b) shot noise + Johnson noise of BP PhCWG photodetector and BP SWGWG photodetector.

Shot noise i_s and Johnson noise i_j are calculated from the dark current using the following equations:

$$(i_s)^2 = 2qI_{dark}\cdot\Delta f \quad \text{(S1)}$$

$$(i_j)^2 = 4k_BT\cdot\Delta f\cdot I_{dark}/V_d \quad \text{(S2)}$$

where q is elementary charge, Δf is the bandwidth, k_B is Boltzmann constant, T is the temperature.

Note S8: Two BP field-effect transistors

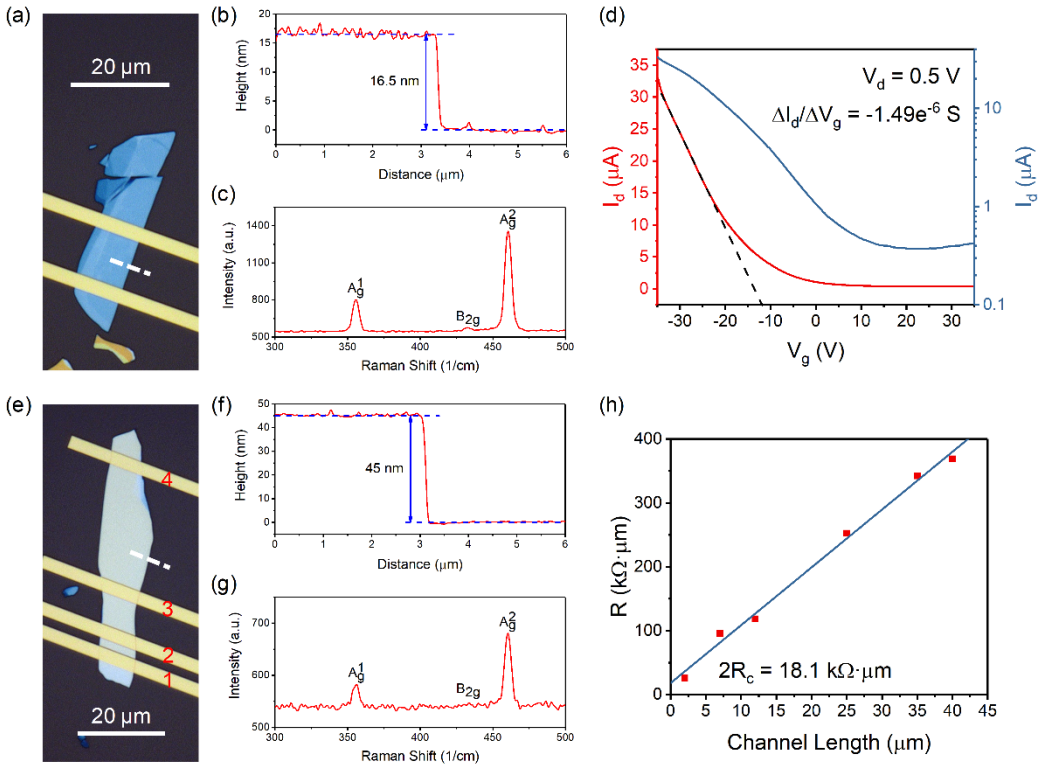

Figure S8. (a-d) Device A. (a) Microscopic image of the fabricated device; (b) AFM height profile of the 16.5 nm thick BP flake along the white dashed line in (a); (c) Raman spectrum of the BP flake, where both the incident laser polarization and the detection polarization are parallel to the white dashed line in (a); (d) Transfer curve under a 0.5 V source-drain bias in linear and log scale. The slope of the linear region is for the extraction of the hole mobility. (e-h) Device B. (e) Microscopic image of the fabricated device; (b) AFM height profile of the 45 nm thick BP flake along the white dashed line in (e); (c) Raman spectrum of the BP flake, where both the incident laser polarization and the detection polarization are parallel to the white dashed line in (e); (h) Transmission line method result under a zero gate bias, from which the contact resistance between Ti/Au electrodes and the BP flake is extracted.

Note S9: Equivalent circuit modelling of device B

Table S2. Parameters for equivalent circuit modeling and the corresponding calculated 3dB bandwidth

Parameter Set No.	R_{BP} **(kΩ)**	R_C **(kΩ)**	C_{BP} **(pF)**	C_P **(fF)**	R_S **(Ω)**	R_L **(Ω)**	f_{3dB} **(Hz)**
1	27.577	1.065	0.077	50	25	50	1.0×10^9
2	27.577	1.065	7.7	50	25	50	1.0×10^7
3	27.577	1.065	770	50	25	50	1.0×10^5
4	27.577	1.065	77000	50	25	50	1.0×10^3

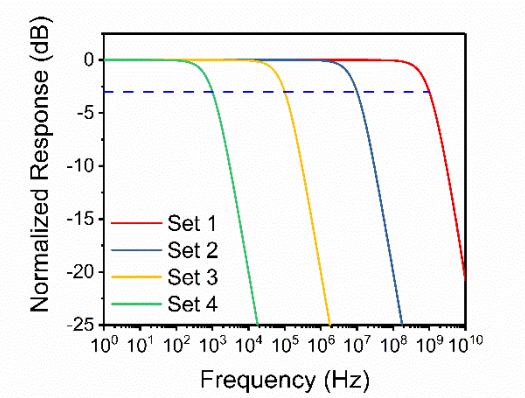

Figure S9. Modeled frequency responses of device B with different parameters as listed in Table S2. The 3-dB bandwidth is dominated by the BP capacitance and decreases at the same scale as the increase of the BP capacitance.

Note S10: Summary of BP waveguide photodetectors

Table S3. Summary of BP waveguide photodetectors

Waveguide Structure	**BP Property**	**Wavelength (μm)**	**Bias (V)**	**Power (μW)**	**Responsivity (A W^{-1})**	***L*** [a] **(μm) × *W*** [b] **(μm)**	**Ref.**
Si strip waveguide	11.5 nm zigzag	1.55	-0.4	1910	0.0188	6.5 × 1.5	[6]
Si waveguide grating	20 nm	1.55	0.7	12.6	0.214	4.5 × 12	[8]
Chalcogenide glass ridge waveguide	32.4 nm zigzag	2.185	0.2	175	0.04	40 × 4.5	[9]
Si grating coupler	40 nm zigzag	3.78	1	1.193	1.333	80 × 14	[10]
Si rib waveguide	48.5 nm armchair	2	0.4	125	0.3067	33.3 × 3.6	[7]
Si photonic crystal waveguide	40 nm zigzag	3.825	0.5	1.118	1.445	10 × 12	This work

[a] L – device length (i.e., channel width); [b] W – device width (i.e., channel length).

Table S3 summarizes the characteristics of reported BP waveguide photodetectors in chronological order, showing a trend that the research focus is gradually migrating from the NIR to the MIR. With the increasing wavelength, the BP absorption weakens and the waveguide dimensions increase. Thanks to the slow light enhancement, our device maintains a high responsivity at a low voltage bias and a short device length. In addition, a shorter channel length can actually shorten the carrier transit time and consequently increase the responsivity.

Note S11: Measurement setups

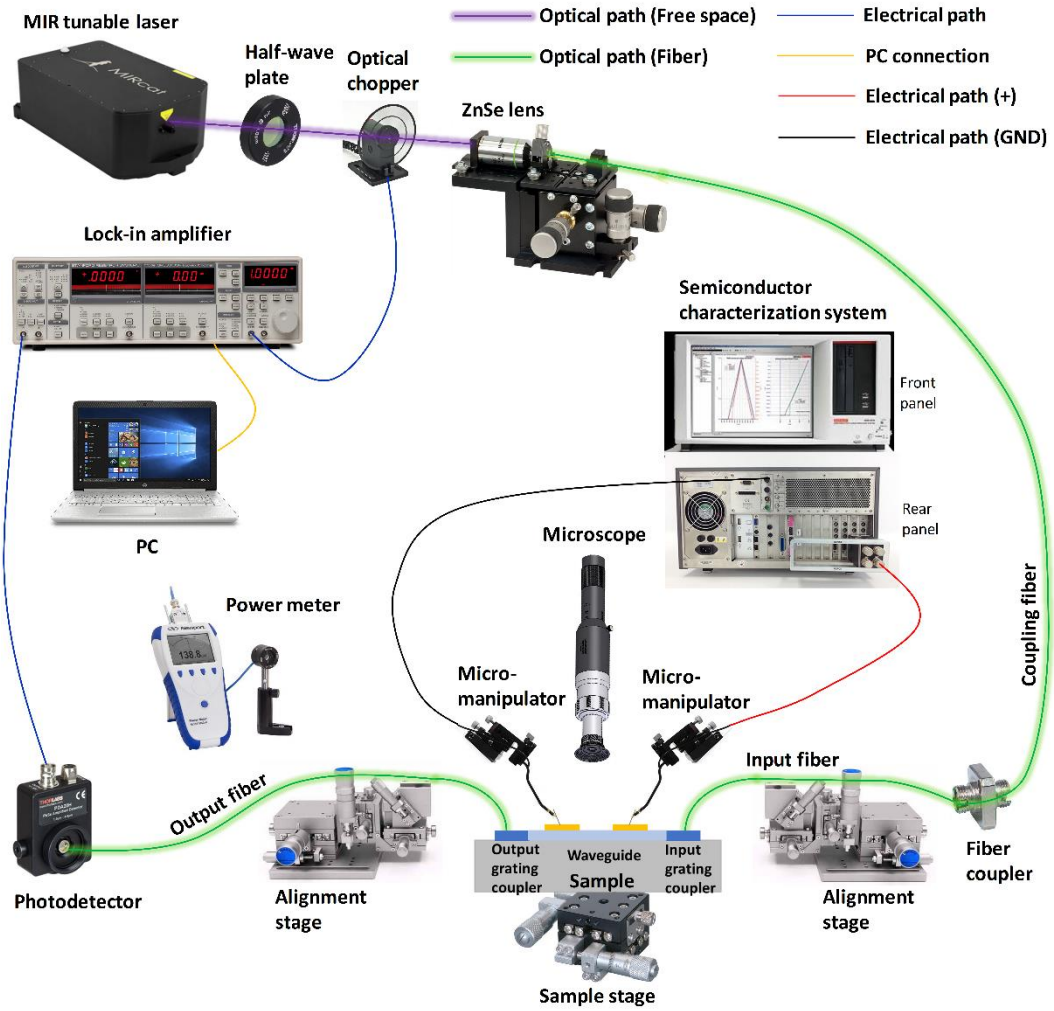

Figure S10. Measurement setup for the photoresponse characterization of the BP waveguide photodetectors.

Figure S10 schematically illustrates the setup for the photoresponse measurement of the BP waveguide photodetectors. The MIR light from the laser source first passes through a half-wave plate with a rotation mount for polarization control and an optical chopper for signal modulation, then is launched into a single-mode fiber by a ZnSe focusing lens. The alignment between the fibers and the grating couplers is performed with the alignment stages and the sample stage. The light coupled to the output fiber is directed to a commercial MIR detector. Both the detector and the chopper are connected to a lock-in amplifier to enhance the SNR of

the output signal. A semiconductor characterization system is used to apply voltage bias to the BP photodetectors and measure the current. One probe is connected to a SMU, and the other probe is connected to the ground unit. The noise power density measurement setup is schematically illustrated in our previous work.[10]

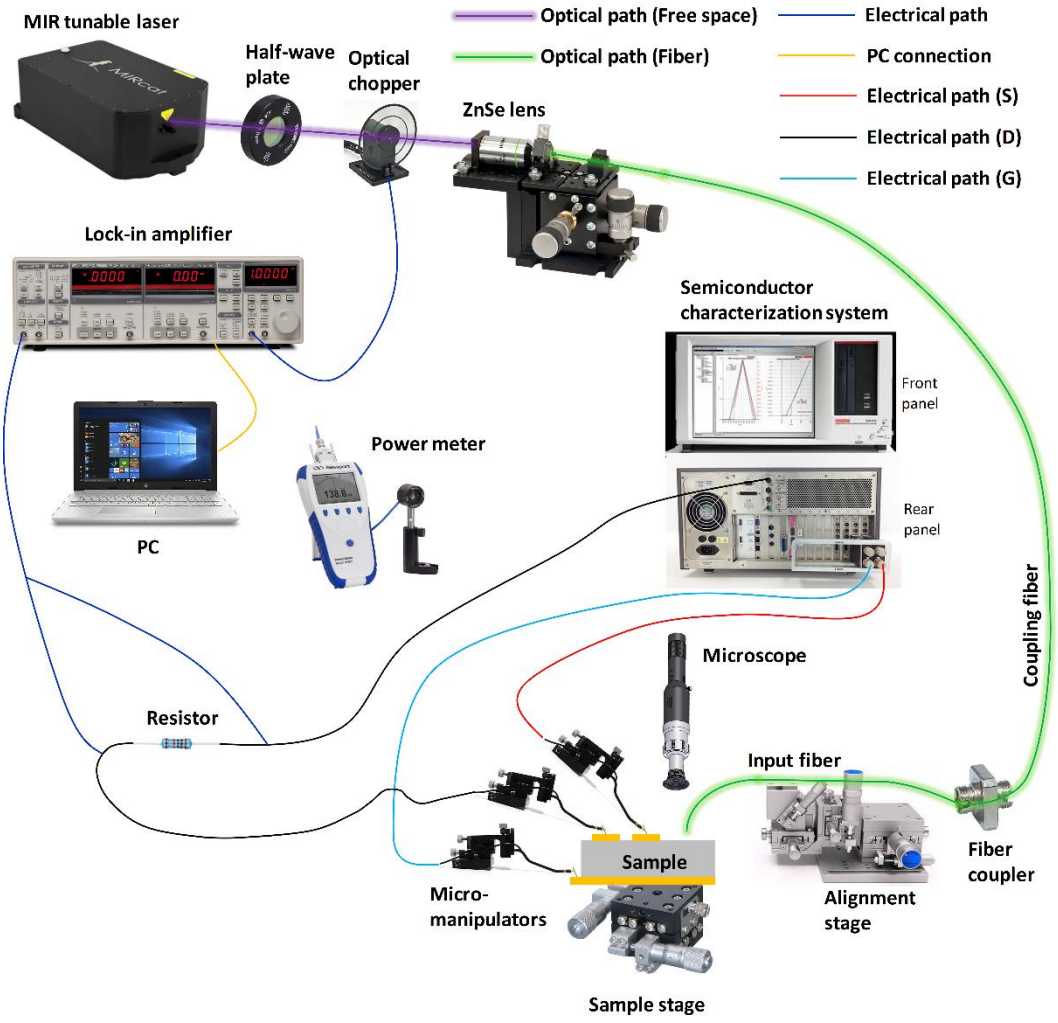

Figure S11. Measurement setup for the photoresponse characterization of the free-space BP photodetectors.

Figure S11 schematically illustrates the setup for the photoresponse measurement of the free-space BP photodetectors. The light is guided above the sample surface with a single-mode fiber. In the frequency response measurement, the light is modulated by the optical chopper

with different frequencies. A standard resistor is connected in series with the sample to convert the photocurrent into voltage signal for the lock-in amplifier to read.

References

[1] Z. Luo, J. Maassen, Y. Deng, Y. Du, R. P. Garrelts, M. S. Lundstrom, P. D. Ye, X. Xu, *Nat. Commun.* **2015**, *6*, 8572.

[2] J. Wu, N. Mao, L. Xie, H. Xu, J. Zhang, *Angew. Chemie - Int. Ed.* **2015**, *54*, 2366.

[3] X. Ling, S. Huang, E. H. Hasdeo, L. Liang, W. M. Parkin, Y. Tatsumi, A. R. T. Nugraha, A. A. Puretzky, P. M. Das, B. G. Sumpter, D. B. Geohegan, J. Kong, R. Saito, M. Drndic, V. Meunier, M. S. Dresselhaus, *Nano Lett.* **2016**, *16*, 2260.

[4] F. Xia, H. Wang, Y. Jia, *Nat. Commun.* **2014**, *5*, 4458.

[5] G. Zhang, S. Huang, A. Chaves, C. Song, V. O. Özçelik, T. Low, H. Yan, *Nat. Commun.* **2017**, *8*, 14071.

[6] N. Youngblood, C. Chen, S. J. Koester, M. Li, *Nat. Photonics* **2015**, *9*, 247.

[7] Y. Yin, R. Cao, J. Guo, C. Liu, J. Li, X. Feng, H. Wang, W. Du, A. Qadir, H. Zhang, Y. Ma, S. Gao, Y. Xu, Y. Shi, L. Tong, D. Dai, *Laser Photon. Rev.* **2019**, *13*, 1900032.

[8] C. Chen, N. Youngblood, R. Peng, D. Yoo, D. A. Mohr, T. W. Johnson, S. H. Oh, M. Li, *Nano Lett.* **2017**, *17*, 985.

[9] S. Deckoff-Jones, H. Lin, D. Kita, H. Zheng, D. Li, W. Zhang, J. Hu, *J. Opt.* **2018**, *20*, 044004.

[10] L. Huang, B. Dong, X. Guo, Y. Chang, N. Chen, X. Huang, W. Liao, C. Zhu, H. Wang, C. Lee, K.-W. Ang, *ACS Nano* **2019**, *13*, 913.